Investigation of AlInAsSb/GaSb tandem cells – A first step towards GaSb-based multi-junction solar cells

J. Kret, J. Tournet, S. Parola, F. Martinez, D. Chemisana, Rémi Morin, M. de La Mata, N. Fernández-Delgado, A.A. Khan, S.I. Molina, et al.

Investigation of AlInAsSb/GaSb tandem cells – A first step towards GaSb-based multi-junction solar cells

J. Kret[a]‡, J. Tournet[a]‡$, S. Parola[a]*, F. Martinez[a], D. Chemisana[b], R. Morin[a], M. de la Mata[c], N. Fernández-Delgado[c], A.A. Khan[c], S.I. Molina[c], Y. Rouillard[a], E. Tournié[a], Y. Cuminal[a]

[a] IES, Univ. Montpellier, CNRS, F- 34000, Montpellier, France

[b] Applied Physics Section of the Environmental Science Department, University of Lleida, Jaume II 69, 25001 Lleida, Spain

[c] Departamento de Ciencia de los Materiales, Ing. Met. y Qca.Inorg., IMEYMAT, Universidad de Cádiz, 11510 Puerto Real, Spain

‡ Equal contribution

[$]Present address: Department of Electronic Materials Engineering, Research School of Physics, The Australian National University, Canberra, ACT 2601, Australia

* *corresponding author:* stephanie.parola@umontpellier.fr

Abstract

III-Sb semiconductors cover the whole 0.29-1.64 eV bandgap range, allowing us to grow several subcells of a multi-junction solar cell lattice-matched to GaSb. Among III-Sb alloys, AlInAsSb exhibits the broadest range of direct bandgaps, making it a promising material for photovoltaic applications. In this work, the behavior of two AlInAsSb/GaSb tandem photovoltaic cells is studied. Material characterization and physics-based 1D modeling are carried out to analyze and discuss performance of the cells. An efficiency of 5.2% is achieved under 1-sun illumination, limited by the AlInAsSb quaternary-alloy properties.

Keywords
GaSb; AlInAsSb; III-Sb alloys; tandem cells; III-V multi-junction solar cells

I. Introduction

GaSb-based alloys are attractive materials for applications in the near-IR spectral range. Particularly, GaSb (0.7 eV) and GaInAsSb (0.5 eV) currently draw scientific attention in the photovoltaic field for the realization of narrow-bandgap absorbers. Initial trials on their mechanical introduction into 4- and 5-junction structures have already been reported making use of GaInAsSb [1,2]. Numerous studies have addressed the optimization of the GaSb solar cell architectures grown either on GaSb [3] or more conventional substrates such as GaAs or Si [4,5]. Although mechanical stacking and wafer bonding offer the possibility of combining subcells originating from different substrates, the fabrication of all-lattice-matched multi-junction solar cells remains the simplest solution. In this context, quaternary III-Sb alloys are promising candidates for the realization of narrow- and medium-bandgap subcells (0.5-1.6 eV). However, the AlInAsSb compositions falling in this range exhibit a large miscibility gap [6], often leading to unstable structures prone to phase separation, even when grown using non-equilibrium techniques [7]. In the case of successful attempts, improvements to the growth conditions are still required to provide an accurate control of the quaternary composition and sufficient material quality, particularly at high Al-contents, *i.e.* high-bandgap alloys [7,8].

The strategy proposed here is to investigate AlInAsSb alloys as the active layer of a medium-bandgap subcell. AlInAsSb has the highest attainable direct bandgap among III-Sb alloys and can be grown lattice-matched to GaSb and InP [9]. It has been extensively studied for InP-based solar cells in literature [10–12], resulting in an efficiency as low as 0.9% delivered by a stand-alone $Al_{0.58}In_{0.42}As_{0.91}Sb_{0.09}$ device under 1 sun AM1.5G illumination [13]. This poor result was attributed to a high absorption of the front grid metal and a short diffusion length of minority

carriers. Our group has previously reported preliminary results on an AlInAsSb/GaSb tandem cell [14]. However, a deeper analysis of the material and device physics is required to evaluate its potential for integration into a multi-junction solar cell.

Herein, we report on the growth, fabrication, characterization and numerical analysis of AlInAsSb/GaSb tandem cells. The target composition of the quaternary alloy is $Al_{0.75}In_{0.25}As_{0.27}Sb_{0.73}$, corresponding to a bandgap value of 1.33 eV. The motivation underlying this choice is that the subcell could be also used as a 3rd and 4th junction in 4- and 6-junction solar cells, respectively. Optimization of the growth and performance of AlInAsSb/GaSb tandem cells is therefore the first step towards a successful development of III-Sb multi-junction solar cells. To begin with, this work focuses on the AlInAsSb alloy characterization carried out to analyze its crystalline structure and to derive the optical and electrical parameters necessary for numerical simulations. The cells performance is then studied by means of 1D modeling and discussed in terms of material quality.

II. Experimental details

The AlInAsSb alloy studied in this work was grown by molecular beam epitaxy (MBE) on epi-ready GaSb (001) substrates. The substrate was deoxidized *in-situ* under Sb flux at 550°C, followed by the deposition at 500°C of a 200 nm-thick GaSb buffer layer. The substrate temperature was determined with a pyrometer calibrated by the (1x3) to (2x5) reconstruction change (which occurs at 415°C under a 1 ML/s Sb-flux [15]). Preliminary analyses, published in [8], allowed us to define suitable growth conditions for AlInAsSb alloys of reasonable quality: growth temperature of 400°C, 1 ML/s growth rate (group III elements) and a V/III beam equivalent pressure (BEP) ratio between 6 and 9. The AlInAsSb alloy was grown as a random alloy, *i.e.* by opening all shutters at the same time, rather than using the digital alloy technique as recently reported in literature [16]. The target composition was $Al_{0.75}In_{0.25}As_{0.27}Sb_{0.73}$. The epitaxy was monitored *in-situ* by reflection high-energy electron diffraction (RHEED). *Ex-situ*, high-resolution X-ray diffraction (HRXRD), scanning transmission electron microscopy (STEM), Hall Effect and ellipsometry measurements were combined to determine and correlate the material properties. The elemental composition was estimated by a combination of RHEED and XRD measurements, and further confirmed by the (S)TEM analysis. The (S)TEM analysis was carried out by the INNANOMAT group at the University of Cadiz and at the Ernst Ruska-Centre for Microscopy and Spectroscopy with Electrons in Jülich. The samples were characterized under high-resolution transmission electron microscopy (HRTEM) and aberration-corrected, high-angle, annular dark field (HAADF) imaging conditions. Energy-dispersive X-ray spectroscopy (EDX) was also used to establish chemical mapping of the distribution of constituents. The optical constants (n, k) of the alloy were determined by spectroscopic ellipsometry using a Sopra ellipsometer (GES-5E). The Tauc-Lorentz and Gaussian oscillator functions were combined to estimate the refraction index and extinction coefficient values of the $Al_{0.75}In_{0.25}As_{0.26}Sb_{0.74}$ sample. Hall Effect measurements using the van der Pauw technique were carried out on an Ecopia HMS-5500 system at 300 K in order to evaluate the electron and hole mobilities of the AlInAsSb layer. Dedicated samples were prepared for these measurements. AlInAsSb layers with 2-3 different doping concentrations (for each doping type) were grown on (001)-oriented semi-insulating GaAs substrates.

Two solar cells, SC1 and SC2, were grown using a similar process (structure depicted in Fig. 1). After deposition of the buffer, the bottom GaSb subcell was grown at 500°C, comprising a 25 nm back surface field (BSF), a 3 µm base and a 100 nm emitter. The temperature was then lowered to 400°C for the remainder of the growth: the 25 nm bottom subcell window, the 20/20 nm GaSb/InAs tunnel junction and the entire AlInAsSb subcell (25 nm BSF, 1.5 µm base, 100 nm emitter and 25 nm window). Tellurium and Beryllium were used for n- and p-type doping, respectively. The final structure was capped with 10 nm of GaSb to prevent oxidation of the high-Al-content alloys. The difference between SC1 and SC2 resides in the quaternary alloy composition. Indeed, as detailed below in the XRD analysis, the growth conditions of SC1 resulted in an AlInAsSb layer under compressive stress, *i.e.* with a smaller lattice parameter than GaSb. For the growth of SC2, we attempted to reduce this lattice mismatch by slightly increasing the As flux. No other growth parameter was changed. After growth, the solar cells were processed in a class 10000 clean room at the *Centrale de Technologie en Micro et Nanoélectronique* of the University of Montpellier, based on an identical protocol. A Ti/Au 30/250 nm-thick front metallic grid was first deposited by electron-beam evaporation. 5 µm-deep trenches were then etched by reactive ion etching to isolate the cells from each other. Afterwards, a 106 nm-thick SiN_x anti-reflective coating (ARC) was deposited by plasma-enhanced chemical vapor deposition on the full wafer and etched above the busbars to allow wiring. Finally, a 5/200 nm-thick Pd/AuGeNi alloy was deposited by sputtering on the whole back surface of the wafer. The individual cells were mounted on TO-8 holders. They were 0.5 cm x 0.5 cm wide.

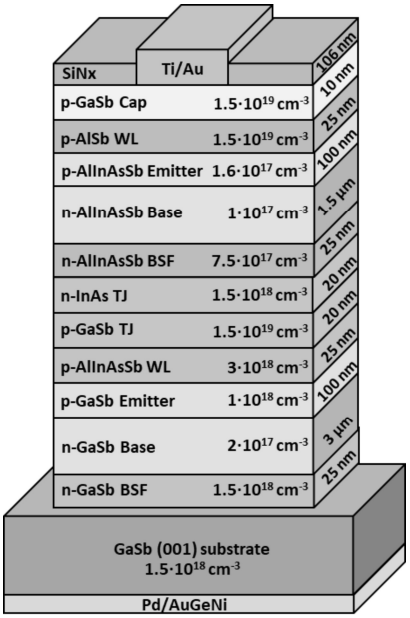

Fig.1 Schematic representation of studied tandem solar cells.

The external quantum efficiency (EQE) setup was composed of an Xe arc lamp (spectral coverage: 350-1800 nm), a monochromator equipped with two gratings, a four-filter wheel blocking higher orders of diffraction and an optical chopper modulating the incident light on the solar cell at a certain frequency. A lock-in amplifier was used for data acquisition. The setup was calibrated using commercial Si and Ge photodiodes. The individual characterization of the tandem subcells required both light and voltage biasing [17,18]. A halogen lamp filtered for $\lambda < 1000$ nm provided infrared optical bias to the bottom subcell while studying the top subcell. Conversely, the top subcell was saturated with a green light source when the bottom subcell was measured. The examined subcell was also maintained under short-circuit conditions by adjusting the external voltage bias to the open circuit voltage of the saturated cell. An additional measurement of the spectral response of the SC2 cell was carried out at the University of Lleida. The measuring setup was based on the same operating principle.

The *J-V* characteristic curves of the solar cells were measured with a Keithley 2400 Source Meter by standard four-point measurements. The solar cells were tested under a Newport ORIEL Sol 3A solar simulator equipped with an AM 1.5G filter. The curves were acquired under both dark and 1 sun illumination conditions. The 1 sun irradiance power was calibrated with regard to the current density of the limiting subcell, as extracted from quantum efficiency measurements and including the impact of the metallic grid shading.

III. Description of the model

One dimension (1D) numerical simulations of multi-junction solar cells are carried out using various in-house developed solvers on the MATLAB platform. According to our previous work, this suite of numerical modeling tools has proven successful for the modeling of GaSb single-junction cells [3]. The model is based on fully-coupled Poisson and continuity equations solved in one direction. A double-valued mesh-points technique is included to account for the heterointerfaces. Bulk recombination mechanisms, *i.e.* Auger, radiative and SRH recombination are considered. Furthermore, the surface recombination velocities are implemented at each layer interface. The device's optical generation is calculated in the entire device *via* the transfer matrix method using the optical properties (n, k) of each layer. The latter are either taken from literature [19,20] (GaSb, InAs, AlSb) or determined experimentally based on ellipsometry measurements (AlInAsSb, SiN_x). Each subcell is individually simulated in this 1D physics-based solvers.

Fig. 2 illustrates the electrical modeling principle of the tandem cells. The tandem cell *J-V* curve was computed with a circuit solver by connecting in series the subcells and a resistor corresponding to the tunnel junction. Indeed, the broken-gap alignment of the GaSb/InAs tunnel junction provides a very low resistance ($R_{tunnel} \sim 4\text{-}5 \cdot 10^{-5}$ $\Omega.cm^2$) [23,24]. Shunt and series resistors are also included, representing the other contributions of resistive losses such as current leakage in mesa edges and series resistances related to contact losses.

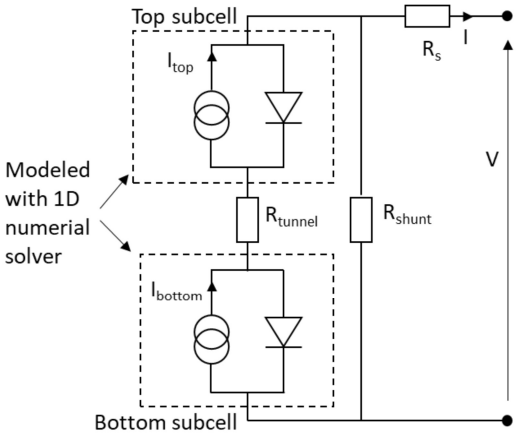

Fig 2. Schematic diagram of the electrical simulation (1D physics-based solver/circuit solver) of tandem cells.

An optimization algorithm, based on the Levenberg-Marquardt method, was used to fit the experimental *J-V* and EQE curves of the tandem cells. The varying parameters are the shunt and series resistances, the density of states for the quaternary compound and the electron and hole SRH lifetimes for both quaternary and GaSb alloys. For a realistic variation range of the input parameters, the algorithm converges towards a single set of values. The material parameters of GaSb and AlInAsSb used for the simulations are summarized in Table I. For GaSb, most of parameters are taken from the literature [19,21]. Due to the lack of experimental data for AlInAsSb, some parameters are estimated from a linear interpolation scheme [22] or assumed to be identical to GaSb (radiative and Auger recombination parameters). The free parameters adjusted for fitting will be discussed in the section V.

Table I. Material parameters used for simulations (at 300 K).

		GaSb	$Al_{0.75}In_{0.25}As_{0.26}Sb_{0.74}$
Electron affinity χ (eV)		4.06 (a) from [19]	3.86 (b) from [22]
Bandgap Eg (eV)		0.726 (a) from [19]	1.33 (c)
Relative permittivity ε_r		15.7 (a) from [19]	12.7 (b) from [22]
Density of states	Nc (cm^{-3})	2.1×10^{17} (a) from [19]	2.0×10^{18} (d)
	Nv (cm^{-3})	1.8×10^{19} (a) from [19]	1.2×10^{20} (d)
Mobility	μ_n (cm^2/V.s)	$850+\frac{5750}{1+\left(\frac{N_d\,(cm^{-3})}{8\cdot10^{17}}\right)^{1.8}}$ (a) from [21]	168 ($N_a=1.6\times10^{17}$ cm^{-3}) (d)
	μ_p (cm^2/V.s)	$85+\frac{1165}{1+\left(\frac{N_d\,(cm^{-3})}{4\cdot10^{17}}\right)^{0.44}}$ (a) from [21]	342 ($N_d=1\times10^{17}$ cm^{-3}) (d)
Recombination parameters	$C_n=C_p$ (cm^6/s)	5×10^{-30} (a) from [19]	5×10^{-30} (e)
	B (cm^3/s)	8.5×10^{-11} (a) from [21]	8.5×10^{-11} (e)
	τ_{SRHe}, τ_{SRHh} (ns)	See Table III. (d)	See Table III. (d)
Surface recombination velocity	at AlInAsSb/GaSb heterointerfaces	$S_n=S_p=10^4$ cm/s (d)	
	at homointerfaces	$S_n=S_p=0$ cm/s (d)	

(a) Material parameters from the literature
(b) Material parameters from a linear interpolation scheme
(c) Material parameters determined from experimental measurements
(d) Free parameters used for fitting
(e) Material parameters assumed to be identical to GaSb due to the lack of data in the literature

IV. Material characterization of AlInAsSb

In this section, structural, optical and electrical characterization of the AlInAsSb alloy are addressed. The data extracted were used as input parameters for the 1D model to help gain a better understanding of tandem cell performance.

A. (S)TEM measurements

The AlInAsSb samples (as-grown and annealed) were characterized using TEM-related techniques. Upon initial observation, the alloy seemed homogeneous and no particular pattern was detected under the microscope. The optical microscope images are provided in the Supplementary Material. The alloy was subsequently annealed for 1h in the MBE reactor (475°C) to test its thermal stability and to reproduce the thermal treatment undergone during the cell processing steps. The chemical composition of the alloy was obtained by means of STEM-EDX analyses (Fig. 3). The EDX data confirmed the overall alloy stoichiometry, which is in agreement with the target value ($Al_{0.75}In_{0.25}As_{0.27}Sb_{0.73}$). Slight deviations of the Al content may be attributed to preferential sample oxidation, mainly affecting the Al species. EDX measurements carried out at higher magnification levels in the annealed sample revealed the alternation of As- and Sb-rich regions with a period of 2-3 nm (6-10 monolayers). Such modulation is further observed when studying the sample under diffraction contrast conditions (two-beams) at selected Bragg reflections, sensitive to chemical variations (Fig. 3b). The As and Sb content variation between consecutive layers is about ± 5%. When paying attention to the Al EDX signal, a modulation can also be inferred. Previous statistical analyses on data obtained by means of atom probe tomography (APT) on these quaternary alloys grown on InP have already revealed small compositional variations at nanometer sub-volumes [11,25], leading to In- and Sb- rich domains within epitaxial layers. Such chemical fluctuations could potentially be hidden or underestimated in the 2D data attainable with (S)TEM measurements. These observations are consistent with a recent study by Lyu *et al*. [26]. The periodic compositional fluctuations were not observed in the non-annealed samples, but their presence should not be discarded (see Supplementary Material). Annealing could increase (pre-)existing compositional fluctuations or induce them by facilitating diffusion. Dim compositional fluctuations may therefore have gone unnoticed in the EDX analyses, requiring more sensitive techniques in order to be detected. It should be noted that solar cell architectures result in long growth times (> 2 h) during which the already-grown material is effectively annealed until the end of the device growth. Thus, it is likely these chemical variations are present in the solar cells shown in the remainder of this work. Such compositional inhomogeneities can induce potential fluctuations that create localized states which can trap the charge carriers and lower their diffusion length [27]. The localized states can impact both the photocurrent density (diffusion length) and open-circuit voltage (bandgap). Compositional inhomogeneities have also been shown to hinder dislocation glide in metamorphic epitaxial growth and could thus lead to an increased defect density, again affecting the carrier diffusion length, hence the cell's current density [28]. More detailed epitaxy and annealing studies remain to be undertaken to improve the quaternary material homogeneity and stability.

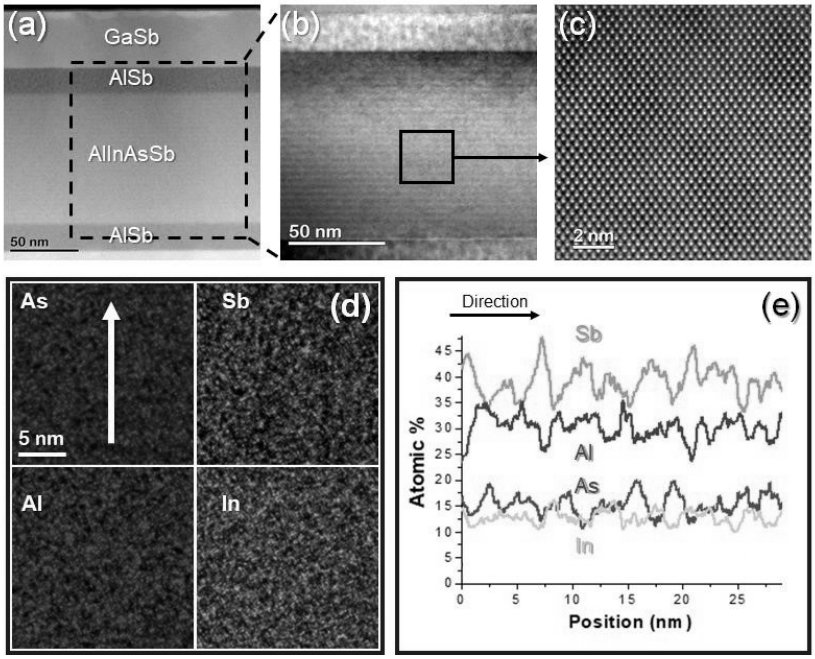

Fig. 3. (S)TEM analysis carried out on the annealed $Al_{0.75}In_{0.25}As_{0.26}Sb_{0.74}$ sample. The Z-contrast image (a) shows the overall architecture, while the diffraction contrast image (b) reveals the periodic chemical modulation of the quaternary alloy. (c) Z-contrast atomic resolution image of the AlInAsSb alloy. (d) EDX results showing the 2D distribution of the constituents in the AlInAsSb layer and (e) an extracted profile along the white arrow in (d), evidencing the chemical modulation.

B. HRXRD measurements

HRXRD analyses of individual AlInAsSb alloys grown at different temperatures have been published previously [8]. Fig. 4 shows in solid lines the ω-2θ scans for the (004) reflections of the AlInAsSb/GaSb solar cells. The data were analyzed with the Panalytical Xpert Epitaxy software (dashed curves in Fig. 4).

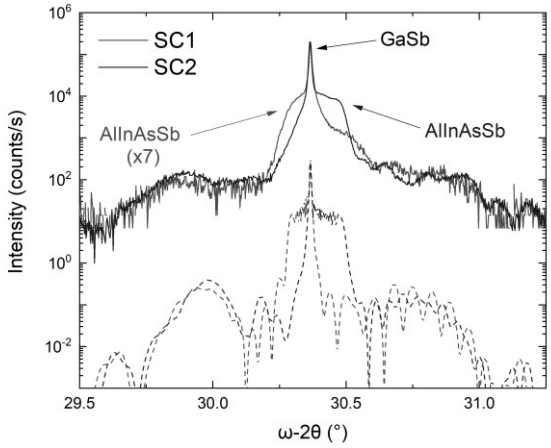

Fig. 4. (004) reflection XRD ω-2θ scans acquired on SC1 (red) and SC2 (blue). Each solar cell includes two subcells, a tunnel junction and a cap layer. The experimental curve of SC1 is up-shifted for clarity. Best fits are down-shifted for clarity and plotted with dashed lines.

The AlInAsSb peaks, corresponding to a thickness of about 1.6 µm, are noticeably broader than the substrate peak with a FWHM of 310" and 520" for SC1 and SC2, respectively. For XRD simulation purposed, we have considered that the AlInAsSb layers underwent a composition gradient: from $Al_{0.75}In_{0.25}As_{0.26}Sb_{0.74}$ to $Al_{0.75}In_{0.25}As_{0.27}Sb_{0.73}$ for SC1 and from $Al_{0.75}In_{0.25}As_{0.27}Sb_{0.73}$ to $Al_{0.75}In_{0.25}As_{0.30}Sb_{0.70}$ for SC2, respectively. Such a composition gradient could be induced by the increasing As background pressure during growth, As being more difficult to pump than other elements in MBE. The XRD simulations presented in Fig. 4 also considered fully strained layers and unity sticking coefficients for the group-III elements. The quaternary alloy in SC1 appears

slightly lattice-mismatched to GaSb ($\Delta a/a = 6.2x10^{-4}$) under compressive stress. SC2 was grown with a slightly increased As flux and the quaternary alloy was, in this case, lattice-mismatched under tensile stress ($\Delta a/a = -5.9x10^{-4}$). This illustrates the extreme sensitivity of the alloy composition to the growth conditions, namely the substrate temperature and As flux, which had already been observed during the calibration growths. Both mismatch values were calculated at room temperature. Taking into consideration the different thermal expansion coefficients, the growth temperature mismatch increases towards the low $(1\text{-}2)x10^{-3}$ range. According to numerous studies on III-V materials, these mismatch values are still generally considered too low to provoke significant stress relaxation [29,30].

Despite our best efforts, the ω-2θ curve fitting does not reproduce the signal very well on the left side of the peak (lower ω-2θ values). This could stem from growth defects and texture that broaden and shift the XRD peaks, preventing good agreement between the fitting and the experimental data. These observations, added to the broader peaks measured, seem to indicate that the crystalline quality of the alloy can still largely be improved. It is worth noting that, usually, the growth of high-quality Al-rich compounds requires high temperatures which cannot be implemented during the AlInAsSb growth due to its miscibility issues.

C. Carrier transport properties

Hall Effect measurements were carried out on dedicated samples composed of AlInAsSb layers with various doping concentrations. The experimental data of electron and hole mobilities of $Al_{0.75}In_{0.25}As_{0.26}Sb_{0.74}$ alloys are shown as a function of doping level in Figs. 5a and b. Ternaries endpoints of the GaSb-lattice matched $Al_xIn_{1-x}As_ySb_{1-y}$ alloy are $InAs_{0.91}Sb_{0.09}$ and $AlAs_{0.08}Sb_{0.92}$ respectively for x=0 and x=1. In the absence of data for these ternary compounds, the data of InAs and AlSb binaries are provided.

These experimental data give a general trend of the variation of the mobility as a function of the doping level for the AlInAsSb quaternary alloy. These results provide reasonable values as starting guess for simulations.

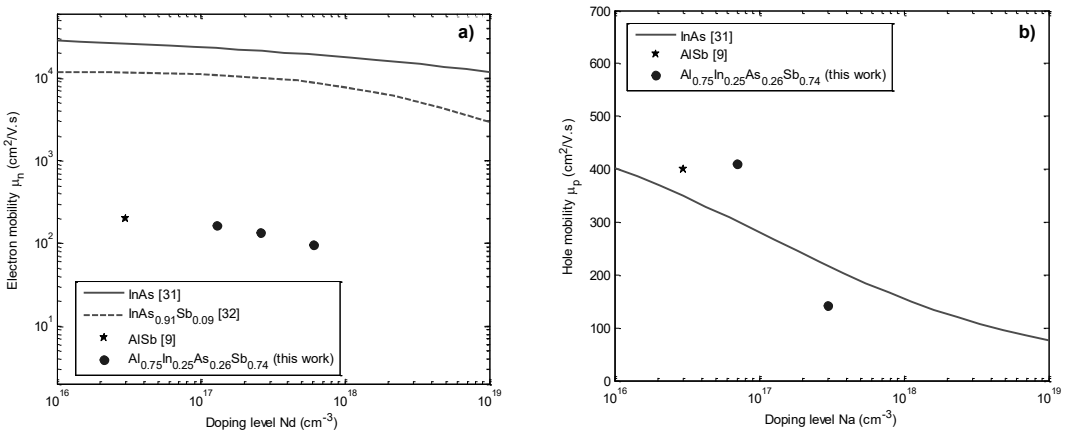

Fig. 5. Experimental data of electron a) and hole b) mobilities of $Al_{0.75}In_{0.25}As_{0.26}Sb_{0.74}$, InAs [31], $InAs_{0.91}Sb_{0.09}$ [32] and AlSb [9] alloys.

D. Ellipsometry measurements

The optical properties of the quaternary compounds were also investigated. The evolution of the refractive index, *n,* as a function of the wavelength, λ, as extracted from the ellipsometry measurements, is depicted in Fig. 6a for AlInAsSb, AlSb and InAs. Fig.6b shows the experimental absorption coefficient of the materials, $\alpha(\lambda)$. As expected, in both cases the AlInAsSb behavior lies between the curves corresponding to the endpoint binary compounds (InAs and AlSb). The optical properties of the quaternary alloy, however, cannot be determined by applying Vegard's law as it fails to estimate the evolution of the absorption band edge. The abrupt decrease in α of around 1.24 eV for AlInAsSb suggests a direct bandgap at this value, in agreement with the value (~ 1.21 eV) presented by Maddox *et al.* [16]. However, a preliminary photoluminescence (PL) study carried out on very thin AlInAsSb layers (50-100 nm-thick) indicated a bandgap situated at 1.33 eV [8]. This discrepancy could be due to the presence of compositional fluctuations, inducing a decrease in the apparent bandgap [13]. These fluctuations have a high impact on thicker layers (1.6 µm), which could explain the difference in bandgap values extracted from the ellipsometry and PL measurements. It is important to note, however, that they do not seem to significantly influence the overall optical properties of this alloy as the presence of a below-bandgap tail has not been detected.

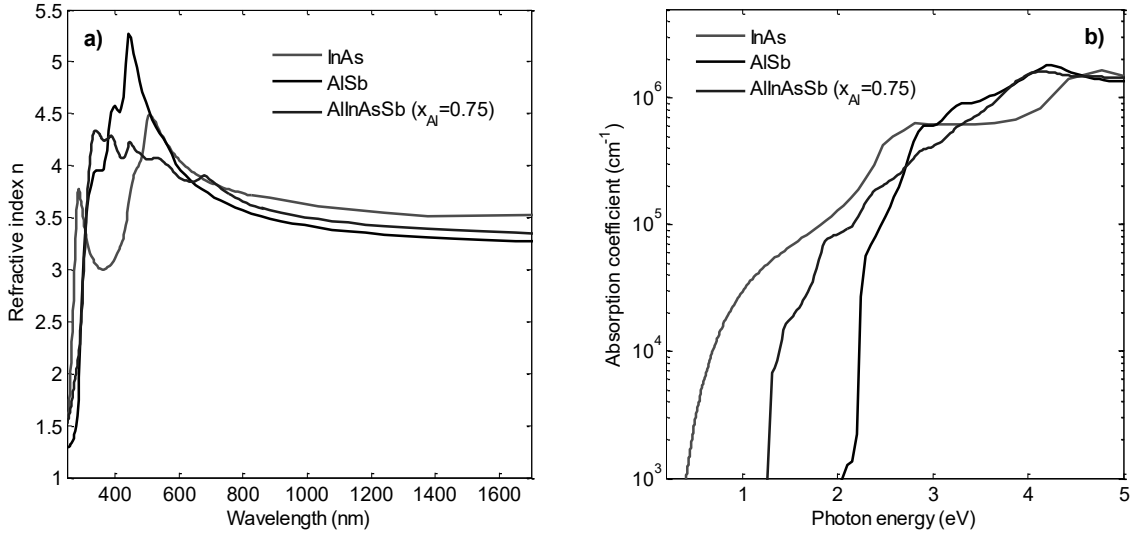

Fig. 6. Optical properties of GaSb-lattice-matched AlInAsSb alloy (x_{Al} = 0.75). The refractive indices a) and absorption coefficients b) of the quaternary compound are presented along with the curves of the endpoint binary compounds (InAs, AlSb) [19,20].

V. Solar cell performance and discussion

Figs. 7a and 7b plot the experimental *J-V* curves of the investigated tandem cells (circles), along with their 1D fits (solid lines). Table II summarizes the figures of merit. As can be noticed, SC2 exhibits a better performance with a conversion efficiency of 5.2%, *vs* 2.3% for SC1, mainly owing to a lower current density generated by SC1.

The comparison of both dark *J-V* curves is shown in Fig. 8. The estimated shunt and series resistances (R_{shunt} and R_s, respectively) are given is Table II. It can be seen that the SC2 cell exhibits a higher reverse dark current density than SC1, due to the lower shunt resistance. The reverse dark current is known to be highly dependent on the leakage current due to perimeter recombination [33]. This effect is exacerbated for small solar cells with high perimeter-to-area ratio. This might be associated with the cleanroom manufacturing process as some steps, such as photolithography or mesa etching, have a considerable impact on the non-passivated sidewalls quality. Hence, it can be concluded that an unintentional manufacturing defect, enhancing the perimeter recombination, was introduced into the SC2 device during cleanroom processing.

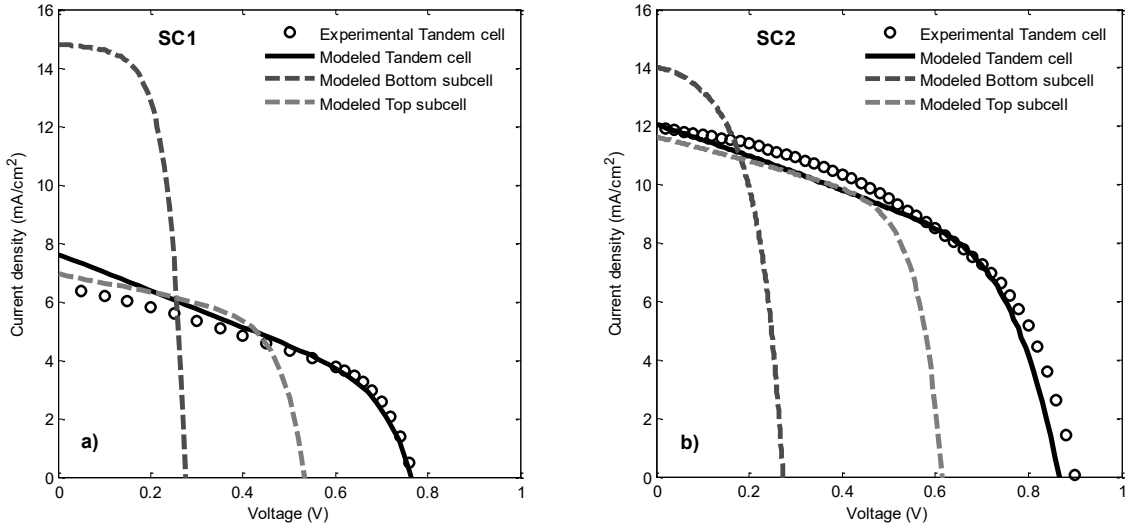

Fig. 7. Experimental (black dots) and modeled (black solid line) *J-V* curves of a) SC1 and b) SC2 cells. The modeled curves of the individual subcells are also presented (colored dashed lines).

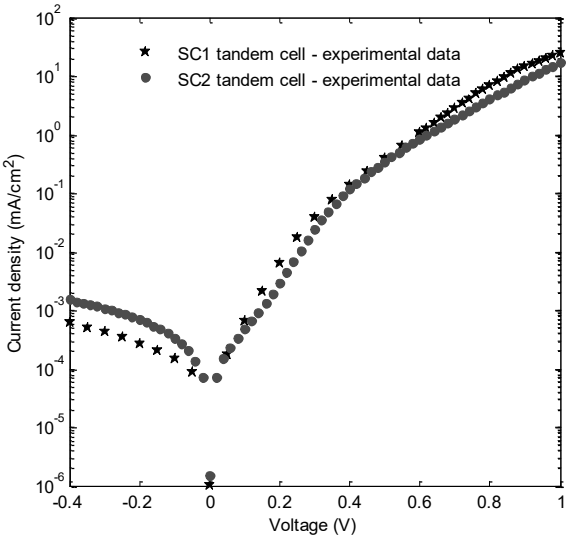

Fig. 8. Experimental dark *J-V* curves of both SC1 and SC2 AlInAsSb/GaSb tandem cells.

Table II. Measured figures of merit for the two tandem cells under 1-sun illumination.

Sample	J_{sc} (mA/cm^2)	V_{oc} (mV)	FF (%)	η (%)	R_s (Ω.cm^2)	R_{shunt} (MΩ.cm^2)
SC1	6.5	769	45	2.3	4	10
SC2	12	904	47.6	5.2	4	0.3

Figs. 9a and 9b illustrate the EQE measurements of SC1 and SC2, respectively, including 1D fits. For the purpose of comparison, Fig. 9b also displays the EQE results obtained at the University of Lleida. Both sets of measurements are in agreement, thereby confirming their accuracy. The EQE curves reveal that in both cases the current generated by the top subcell limits the overall performance of the tandem cell. In particular, a significantly unbalanced current is found for SC1, whereby the GaSb subcell produces almost 2.5 times higher current density than the AlInAsSb subcell. This disparity is significantly reduced in the case of SC2.

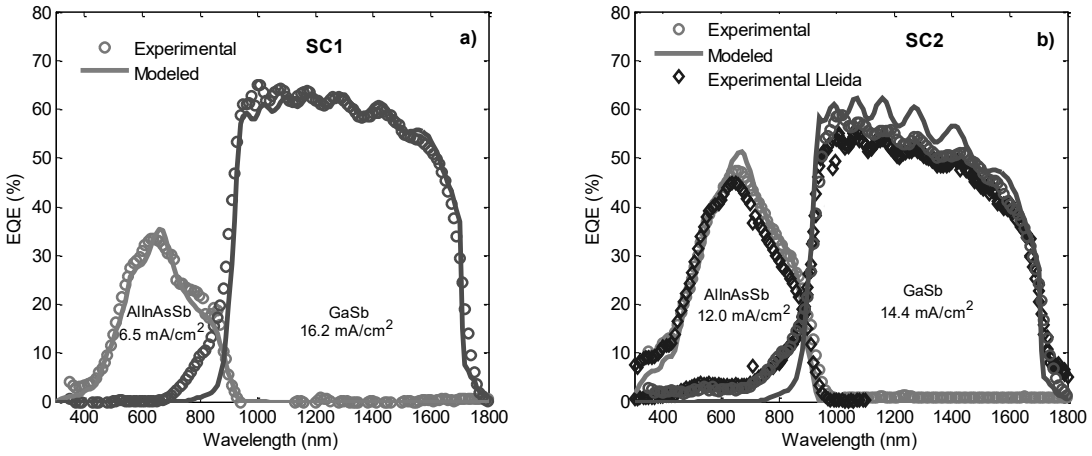

Fig. 9. Experimental (dots) and modeled (solid lines) EQE measurements of the top and bottom subcells of a) SC1 and b) SC2.

1D numerical simulations were carried out in order to provide a deeper understanding of the origin of the factors limiting the performance of individual subcells. Good agreement between the modeled and experimental curves was obtained by adjusting the densities of states and the mobilities of the $Al_{0.75}In_{0.25}As_{0.26}Sb_{0.74}$ alloy (given

in Table I), as well as the carrier lifetimes (summarized in Table III). Same values of mobilities are used for both samples. These values are consistent with the experimental values estimated from Hall effect measurements. It can be noted that, for both tandem cells, the carrier lifetimes extracted for AlInAsSb (in the order of picoseconds) are significantly poorer than those for GaSb (in nanoseconds). These low values are due to the presence of deep level defects in the quaternary alloy, acting as recombination centers. This is corroborated by previous PL measurements, whereby the $Al_{0.75}In_{0.25}As_{0.26}Sb_{0.74}$ alloy exhibited no signal at room temperature suggesting high non-radiative recombination rates [8]. It has already been demonstrated that Al-rich alloys are prone to a fast and unintentional incorporation of oxygen leading to the creation of numerous deep level defects [34]. The extracted AlInAsSb lifetimes correspond to the minority carrier diffusion lengths of 50 nm and 100 nm in the SC1 and SC2 absorbers, respectively, which is of the same order of magnitude as the value reported in [13]. Moreover, it is worth noting that the depletion region also contributes to the current production and spreads over about 900-1000 nm in the base of the top subcells.

Interestingly, a minor difference in the efficiency of the bottom subcells can also be observed despite the similar architecture. The GaSb subcell generates a current density of 16.2 mA/cm^2 and 14.4 mA/cm^2 in SC1 and SC2, respectively. As can be observed from the EQE curves, the SC2 cell exhibits a more inclined plateau region, indicating a poorer carrier collection for long wavelengths. Consequently, the extracted bulk lifetime in the base of the SC2 bottom subcell is lower than in SC1. It is noteworthy that a 1D model does not allow us to dissociate the bulk recombination from the perimeter recombination related to the surface recombination occurring at the mesa sidewalls. We believe that the difference in performance is unlikely due to bulk recombination. The difference between lifetime values could be more likely induced by manufacturing defects generated during clean room processing (surface contamination, material contamination by diffusion, non-ideal sidewalls passivation, etc…). However, the exact nature of the difference cannot be explained at this time and requires further investigations.

Due to low SRH bulk lifetimes found for AlInAsSb and GaSb, the Surface Recombination Velocities (SRV) at the interfaces of constituent layers do not affect the *J-V* curves. This suggests that their value is low (< 10^4 cm/s), which is in agreement with the values reported for III-Sb compounds [35].

The AlInAsSb optical constants estimated from ellipsometry measurements are used to model the optical generation taking place within both tandem cells. The discrepancy between the modeled and experimental EQE of the bottom subcells could possibly be attributed to a slightly overestimated absorption of the quaternary alloy over the 700-900 nm wavelength range.

Table III. SRH lifetimes extracted from 1D numerical simulations.

Sample	$\tau_{SRH,e}$ (AlInAsSb)	$\tau_{SRH,h}$ (AlInAsSb)	$\tau_{SRH,e}$ (GaSb)	$\tau_{SRH,h}$ (GaSb)
SC1	0.5 ps	3 ps	0.5 ns	2 ns
SC2	0.5 ps	10 ps	0.2 ns	3.3 ns

VI. Conclusion

This work reports on the experimental results of AlInAsSb/GaSb tandem solar cells and the corresponding AlInAsSb epilayers characterization. The solar cells performance levels are analyzed by means of 1D physical modeling. It is demonstrated that the current produced by the AlInAsSb top subcells restricts the global performance of the tandem cells. This limitation is attributed to high carrier-recombination rates within the quaternary epilayers. Thus, the crystal quality of AlInAsSb remains to be improved in order to provide photovoltaic-grade material. Until then, the digital alloy growth technique remains the most promising approach, by providing better control over the alloy composition. Beyond necessary technological improvements, the promising efficiency of 5.2% paves the way to the use of AlInAsSb alloys in GaSb lattice-matched, multi-junction solar cells.

Acknowledgment

This work was partly supported by the French program on “Investments for the future” managed by the National Agency for Research under contracts ANR-10-LABX-22-01-SOLSTICE and ANR-11-EQPX-0016 (Equipex EXTRA) and the H2020 program through MSCA ITN PROMIS (GA 641899). Junta de Andalucía (PAI

research group TEP-946 INNANOMAT) is also acknowledged. MdlM thanks Juan de la Cierva postdoctodal contract (IJCI-2017-31507). We thank Prof. Rafal E. Dunin-Borkowski for providing access to the FEI Titan G2 80-200 ChemiSTEM microscope of Ernst Ruska-Centre for Microscopy and Spectroscopy with Electrons.

References

[1] F. Dimroth, T.N.D. Tibbits, M. Niemeyer, F. Predan, P. Beutel, C. Karcher, E. Oliva, G. Siefer, D. Lackner, P. Fuß-kailuweit, A.W. Bett, R. Krause, C. Drazek, E. Guiot, J. Wasselin, A. Tauzin, T. Signamarcheix, Four-Junction Wafer-Bonded Concentrator, IEEE J. Photovoltaics. 6 (2016) 343–349. https://doi.org/10.1109/PVSC.2015.7356148.

[2] M.P. Lumb, S. Mack, K.J. Schmieder, M. González, M.F. Bennett, D. Scheiman, M. Meitl, B. Fisher, S. Burroughs, K.T. Lee, J.A. Rogers, R.J. Walters, GaSb-Based Solar Cells for Full Solar Spectrum Energy Harvesting, Adv. Energy Mater. 7 (2017) 1–9. https://doi.org/10.1002/aenm.201700345.

[3] S. Parola, A. Vauthelin, J. Tournet, J. Kret, J. El Husseini, F. Martinez, Y. Rouillard, E. Tournié, Y. Cuminal, Improved efficiency of GaSb solar cells using an Al0.50Ga0.50As0.04Sb0.96 window layer, Sol. Energy Mater. Sol. Cells. 200 (2019) 110042. https://doi.org/10.1016/j.solmat.2019.110042.

[4] G.T. Nelson, B.-C. Juang, M.A. Slocum, Z.S. Bittner, R.B. Laghumavarapu, D.L. Huffaker, S.M. Hubbard, GaSb solar cells grown on GaAs via interfacial misfit arrays for use in the III-Sb multi-junction cell, Appl. Phys. Lett. 111 (2017). https://doi.org/10.1063/1.4991548.

[5] J. Tournet, S. Parola, A. Vauthelin, F. Martinez, Y. Cuminal, Y. Rouillard, E. Tournié, GaSb Solar Cells for Multi-junction Solar Cell Integration on Si substrates, Sol. Energy Mater. Sol. Cells. 191 (2019) 444–450. https://doi.org/10.1016/j.solmat.2018.11.035.

[6] K. Onabe, Unstable regions in III–V quaternary solid solutions composition plane calculated with strictly regular solution approximation, Jpn. J. Appl. Phys. 21 (1982) L323–L325. https://doi.org/10.1143/JJAP.21.L323.

[7] A.N. Semenov, V.A. Solov'Ev, B.Y. Meltser, Y. V. Terent'Ev, L.G. Prokopova, S. V. Ivanov, Molecular beam epitaxy of AlInAsSb alloys near the miscibility gap boundary, J. Cryst. Growth. 278 (2005) 203–208. https://doi.org/10.1016/j.jcrysgro.2005.01.007.

[8] J. Tournet, Y. Rouillard, E. Tournié, Growth and characterization of AlInAsSb layers lattice-matched to GaSb, J. Cryst. Growth. (2017) 1–5. https://doi.org/10.1016/j.jcrysgro.2017.04.001.

[9] S. Adachi, Properties of Semiconductor Alloys : Group-IV , III – V and II – VI Semiconductors, John Wiley & Sons, Ltd., 2009. https://doi.org/10.1002/9780470744383.

[10] M.P. Lumb, M. Gonzalez, I. Vurgaftman, J.R. Meyer, J. Abell, M. Yakes, R. Hoheisel, J.G. Tischler, P.P. Jenkins, N. Paul, Simulation of novel InAlAsSb solar cells, in: Proc. SPIE, 2012: pp. 1–13. https://doi.org/10.1117/12.909324.

[11] J. Hernández-Saz, M. Herrera, F.J. Delgado, S. Duguay, T. Philippe, M. Gonzalez, J. Abell, R.J. Walters, S.I. Molina, Atom-scale compositional distribution in InAlAsSb-based triple junction solar cells by atom probe tomography, Nanotechnology. 27 (2016) 1–6. https://doi.org/10.1088/0957-4484/27/30/305402.

[12] N. Baladés, M. Herrera, D.L. Sales, F.J. Delgado, D. Hernández-Maldonado, Q.M. Ramasse, J. Pizarro, P. Galindo, M. González, J. Abell, S. Tomasulo, J.R. Walters, S.I. Molina, Structural characterization of InAlAsSb/InGaAs/InP heterostructures for solar cells, Appl. Surf. Sci. 395 (2017) 98–104. https://doi.org/10.1016/j.apsusc.2016.07.094.

[13] M.P. Lumb, M. González, J. Abell, K.J. Schmieder, J.G. Tischler, D.A. Scheiman, M.K. Yakes, I. Vurgaftman, J.R. Meyer, R.J. Walters, Characterization, modeling and analysis of InAlAsSb Schottky barrier solar cells grown on InP, 2014 IEEE 40th Photovolt. Spec. Conf. PVSC 2014. 2 (2014) 243–246. https://doi.org/10.1109/PVSC.2014.6925668.

[14] J. Tournet, Y. Rouillard, E. Tournié, AlInAsSb for GaSb-based multi-junction solar cells, Proc. SPIE. 10527 (2018). https://doi.org/10.1117/12.2289791.

[15] A.S. Bracker, M.J. Yang, B.R. Bennett, J.C. Culbertson, W.J. Moore, Surface reconstruction phase diagrams for InAs, AlSb, and GaSb, J. Cryst. Growth. 220 (2000) 384–392. https://doi.org/10.1016/S0022-0248(00)00871-X.

[16] S.J. Maddox, S.D. March, S.R. Bank, Broadly Tunable AlInAsSb Digital Alloys Grown on GaSb, Cryst. Growth Des. 16 (2016) 3582–3586. https://doi.org/10.1021/acs.cgd.5b01515.

[17] J. Burdick, T. Glatfelter, Spectral response and I-V measurements of tandem amorphous-silicon alloy solar cells,

Sol. Cells. 18 (1986) 301–314. https://doi.org/10.1016/0379-6787(86)90129-8.

[18] M. Meusel, C. Baur, G. Létay, A.W. Bett, W. Warta, E. Fernandez, Spectral response measurements of monolithic GaInP/Ga(In)As/Ge triple-junction solar cells: Measurement artifacts and their explanation, Prog. Photovoltaics Res. Appl. 11 (2003) 499–514. https://doi.org/10.1002/pip.514.

[19] M. Levinshtein, S. Sumyantsev, M. Shur, Handbook series on semiconductor parameters. Volume 1, World Scientific, 1999. https://doi.org/10.1142/9789812832078_0001.

[20] S. Zollner, C. Lin, E. Schönherr, A. Böhringer, M. Cardona, The dielectric function of AlSb from 1.4 to 5.8 eV determined by spectroscopic ellipsometry, J. Appl. Phys. 66 (1989) 383–387. https://doi.org/10.1063/1.343888.

[21] L. Tang, L.M. Fraas, Z. Liu, C. Xu, X. Chen, Performance Improvement of the GaSb Thermophotovoltaic Cells With n-Type Emitters, IEEE Trans. Electron Devices. 62 (2015) 2809–2815. https://doi.org/10.1109/TED.2015.2455075.

[22] S. Adachi, Handbook of Electronic and Photonic Materials - III-V Ternary and Quaternary Compounds, 2017. https://doi.org/10.1007/978-3-319-48933-9.

[23] O. Dier, M. Sterkel, M. Grau, Lin Chun, C. Lauer, M.C. Amann, Tunnel junctions for ohmic intra-device contacts on GaSb-substrates, Appl. Phys. Lett. 85 (2004) 2388–2389. https://doi.org/10.1063/1.1793349.

[24] D. Sanchez, L. Cerutti, E. Tournié, Selective lateral etching of InAs/GaSb tunnel junctions for mid-infrared photonics, Semicond. Sci. Technol. 27 (2012) 085011. https://doi.org/10.1088/0268-1242/27/8/085011.

[25] J. Hernández-Saz, M. Herrera, J. Pizarro, M. Gonzalez, J. Abell, R. Walters, P.L. Galindo, S. Duguay, S.I. Molina, Effect of the thermal annealing and the nominal composition in the elemental distribution of InxAl1-xAsySb1-y for triple junction solar cells, J. Alloys Compd. 792 (2019) 1021–1027. https://doi.org/10.1016/j.jallcom.2019.04.119.

[26] Y. Lyu, X. Han, Y. Sun, Z. Jiang, C. Guo, W. Xiang, Y. Dong, J. Cui, Y. Yao, D. Jiang, G. Wang, Y. Xu, Z. Niu, Digitally grown AlInAsSb for high gain separate absorption, grading, charge, and multiplication avalanche photodiodes, J. Cryst. Growth. 482 (2018) 70–74. https://doi.org/10.1117/12.909324.

[27] L.C. Hirst, M.P. Lumb, J. Abell, C.T. Ellis, J.G. Tischler, I. Vurgaftman, J.R. Meyer, R.J. Walters, M. González, Spatially indirect radiative recombination in InAlAsSb grown lattice-matched to InP by molecular beam epitaxy, J. Appl. Phys. 117 (2015). https://doi.org/10.1063/1.4921883.

[28] C.J.K. Richardson, M.L. Lee, Metamorphic epitaxial materials, MRS Bull. 41 (2016) 193–198. https://doi.org/10.1557/mrs.2016.7.

[29] P. Franzosi, G. Salviati, F. Genova, A. Stano, F. Taiariol, Misfit dislocations in InGaAs/InP MBE single heterostructures, J. Cryst. Growth. 75 (1986) 521–534. https://doi.org/10.1016/0022-0248(86)90098-9.

[30] J.L. Lazzari, C. Fouillant, P. Grunberg, J. Leclercq, A. Jouillé, C. Schiller, Critical layer thickness in AlGaAsSb / GaSb heterostructures determined by X-ray diffraction, J. Cryst. Growth. 130 (1993) 96–100.

[31] M. Sotoodeh, A.H. Khalid, A.A. Rezazadeh, Empirical low-field mobility model for III-V compounds applicable in device simulation codes, J. Appl. Phys. 87 (2000) 2890–2900. https://doi.org/10.1063/1.372274.

[32] Ł. Piskorski, R.P. Sarzała, Material parameters of antimonides and amorphous materials for modelling the mid-infrared lasers, Opt. Appl. 46 (2016) 227–240. https://doi.org/10.5277/oa160207.

[33] H.S. Kim, E. Plis, A. Khoshakhlagh, S. Myers, N. Gautam, Y.D. Sharma, L.R. Dawson, S. Krishna, S.J. Lee, S.K. Noh, Performance improvement of InAs/GaSb strained layer superlattice detectors by reducing surface leakage currents with SU-8 passivation, Appl. Phys. Lett. 96 (2010). https://doi.org/10.1063/1.3275711.

[34] C. Amano, K. Ando, M. Yamaguchi, The effect of oxygen on the properties of AlGaAs solar cells grown by molecular-beam epitaxy, J. Appl. Phys. 63 (1988) 2853–2856. https://doi.org/10.1063/1.340938.

[35] C.A. Wang, D.A. Shiau, D. Donetsky, S. Anikeev, G. Belenky, S. Luryi, Extremely low surface recombination velocity in GaInAsSbAlGaAsSb heterostructures, Appl. Phys. Lett. 86 (2005) 1–3. https://doi.org/10.1063/1.1873042.